

*promoting access to White Rose research papers*



**Universities of Leeds, Sheffield and York**  
**<http://eprints.whiterose.ac.uk/>**

---

This is an author produced version of a paper published in **Earth and Planetary Science Letters**

White Rose Research Online URL for this paper:

<http://eprints.whiterose.ac.uk/id/eprint/77693>

---

**Paper:**

Ammann, MW, Walker, AM, Stackhouse, S, Wookey, J, Forte, AM, Brodholt, JP and Dobson, DP (2014) *Variation of thermal conductivity and heat flux at the Earth's core mantle boundary*. Earth and Planetary Science Letters, 390. 175 - 185 (11). ISSN 0012-821X

<http://dx.doi.org/10.1016/j.epsl.2014.01.009>

---

# Variation of thermal conductivity and heat flux at the Earth's core mantle boundary <sup>1</sup>

Michael W. Ammann <sup>a</sup> Andrew M. Walker <sup>b,c,\*</sup>

Stephen Stackhouse <sup>c</sup> James Wookey <sup>b</sup> Alessandro M. Forte <sup>d</sup>

John P. Brodholt <sup>a</sup> David P. Dobson <sup>a</sup>

<sup>a</sup>*Department of Earth Sciences, University College London, Gower Street, London, WC1E 6BT, UK*

<sup>b</sup>*School of Earth Sciences, University of Bristol, Wills Memorial Building, Queen's Road, Bristol, BS8 1RJ, UK*

<sup>c</sup>*School of Earth and Environment, University of Leeds, Leeds, LS2 9JT, UK*

<sup>d</sup>*GEOTOP - Dépt. Sci. Terre & Atmosphère, Université du Québec à Montréal, CP 8888 succursale Centre-Ville, Montréal QC, H3C 3P8, Canada.*

---

## Highlights

- The thermal conductivity of post-perovskite is 50% larger than that of perovskite.
- Enhanced heat flux into cold regions of D'' where post-perovskite is stable.
- The conductivity of post-perovskite is anisotropic and thus varies with texture.
- Potential for feedback between convection, deformation and conduction in D''.

---

1 **Abstract**

2 The two convective systems that dominate Earth's internal dynamics meet at the  
3 boundary between the rocky mantle and metallic liquid core. Energy transfer be-  
4 tween processes driving plate tectonics and the geodynamo is controlled by thermal  
5 conduction in the lowermost mantle ( $D''$ ). We use atomic scale simulations to deter-  
6 mine the thermal conductivity of  $\text{MgSiO}_3$  perovskite and post-perovskite under  $D''$   
7 conditions and probe how these two convective systems interact. We show that the  
8 thermal conductivity of post-perovskite ( $\sim 12$  W/mK) is 50% larger than that of  
9 perovskite under the same conditions ( $\sim 8.5$  W/mK) and is anisotropic, with con-  
10 ductivity along the  $a$ -axis being 40% higher than conductivity along the  $c$ -axis. This  
11 enhances the high heat flux into cold regions of  $D''$  where post-perovskite is stable,  
12 strengthening the feedback between convection in the core and mantle. Reminiscent  
13 of the situation in the lithosphere, there is potential for deformation induced tex-  
14 turing associated with mantle convection to modify how the mantle is heated from  
15 below. We test this by coupling our atomic scale results to models of texture in  $D''$   
16 and suggest that anisotropic thermal conductivity may help to stabilise the roots of  
17 mantle plumes over their protracted lifetime.

18 *Key words:* Lowermost mantle, Thermal conductivity, Perovskite,  
19 Post-perovskite,  $D''$ , CMB heat flux

---

\* Corresponding author.

*Email address:* [a.walker@leeds.ac.uk](mailto:a.walker@leeds.ac.uk) (Andrew M. Walker).

<sup>1</sup> NOTICE: this is the authors version of a work that was accepted for publication in Earth and Planetary Science Letters. Changes resulting from the publishing process, such as peer review, editing, corrections, structural formatting, and other quality control mechanisms may not be reflected in this document. Changes may have been made to this work since it was submitted for publication. A definitive version was subsequently published in Earth and Planetary Science Letters, [vol. 390, pp. 175-185, (2014)] DOI:10.1016/j.epsl.2014.01.009

## 20 1 Introduction

21 Thermal interaction between the core and mantle is central to our under-  
22 standing of the Earth’s energy budget (Gubbins, 2003; Lay et al., 2008). In  
23 the absence of substantial chemical mixing heat is only transported across the  
24 core mantle boundary (CMB) by conduction in the lowermost mantle ( $D''$ ).  
25 The rate of cooling of the top of the core and heating of the base of the man-  
26 tle is therefore controlled by the temperature difference between the core and  
27 the interior of the mantle and the thermal conductivity of materials such as  
28  $(\text{Mg,Fe})\text{SiO}_3$  perovskite and post-perovskite found in  $D''$ . However, the ther-  
29 mal conductivity of these materials under high pressure ( $P \sim 135$  GPa) and  
30 temperature ( $T \sim 2000\text{--}4000$  K) conditions is unknown. Historically, estimates  
31 of thermal conductivities at the CMB from low pressure or low temperature  
32 experiments, theoretical considerations and extrapolations are 4–29 W/mK  
33 (e.g. Osako and Ito, 1991; Hofmeister, 1999, 2008). Ongoing experimental  
34 work is aimed at refining these estimates but, as yet, it is still not possible  
35 to measure thermal conductivity under the conditions of simultaneously high  
36  $P$  and  $T$  found at the CMB. Manthilake et al. (2011) performed measure-  
37 ments on  $\text{MgSiO}_3$  perovskite and  $\text{MgO}$  to 14 GPa and 1273 K in a multi-anvil  
38 cell. Goncharov et al. (2009) and Dalton et al. (2013) measured the thermal  
39 conductivity of  $\text{MgO}$  at 300K to 32 GPa and 60 GPa, respectively, using a  
40 diamond anvil cell to generate pressure. Goncharov et al. (2010) performed a  
41 similar experiment on perovskite at 125 GPa and 300 K. The latest experi-  
42 mental results (Ohta et al., 2012) reach 144 GPa and include both  $\text{MgSiO}_3$   
43 perovskite and post-perovskite but are limited to near-ambient temperatures  
44 (300–436 K). These results reveal that post-perovskite has  $\sim 60\%$  larger con-

45 ductivity than perovskite and that the conductivity of perovskite increases  
46 from 8 to 37 W/mK as pressure increases from 8 to 144 GPa.

47 Recently, to avoid the formidable experimental challenges in determining ther-  
48 mal conductivity to high pressure and temperature, considerable effort has  
49 been expended in the development of tools to make use of atomic scale sim-  
50 ulations to calculate the thermal conductivity of lower mantle phases. Much  
51 of this work, reviewed by Stackhouse and Stixrude (2010), has focused on  
52 MgO where a range of different techniques have been used. For example, Co-  
53 hen (1998) made use of equilibrium molecular dynamics (MD), interatomic  
54 potentials and Green-Kubo theory, Tang and Dong (2009) used anharmonic  
55 lattice dynamics (LD) truncated to third-order and density functional theory  
56 (DFT), de Koker (2009, 2010) combined DFT, MD and LD in the harmonic  
57 approximation, and Stackhouse et al. (2010) used DFT and non-equilibrium  
58 molecular dynamics (NEMD). Importantly, results of these studies are broadly  
59 in agreement with each other, and with the available experimental data (see  
60 Stackhouse and Stixrude, 2010, Figure 6).

61 There has been less attention focused on MgSiO<sub>3</sub> perovskite or post-perovskite,  
62 despite these phases dominating the mineralogy of the lower mantle and D'',  
63 respectively. As discussed below Stackhouse et al. (2009) reported preliminary  
64 results for perovskite using DFT and NEMD. Very recently Haigis et al. (2012)  
65 used an interatomic potential model, MD and Green-Kubo theory to predict  
66 the thermal conductivity of MgO and the two MgSiO<sub>3</sub> phases to CMB con-  
67 ditions while Dekura et al. (2013) made use of anharmonic LD and DFT to  
68 probe the conductivity of perovskite. At low temperature the results of Haigis  
69 et al. (2012) give thermal conductivities substantially higher than the available  
70 experimental data and these authors appeal to an isotopic correction to reduce

71 their calculated conductivities to values in better agreement with experiment  
72 (phonon scattering by atoms with a mass different to their replicas in adjacent  
73 unit cells will reduce the thermal conductivity). However, an isotopic correc-  
74 tion is not applied by Cohen (1998), de Koker (2009, 2010) or Stackhouse  
75 et al. (2010) but their results for MgO are in reasonable agreement with the  
76 experiments (although the focus is not always on the low temperature proper-  
77 ties where isotopic effects are most important). The LD calculations (Dekura  
78 et al., 2013) give good agreement with experiment at low temperature but  
79 the results deviate from the experiments of Manthilake et al. (2011) at higher  
80 temperatures. There is clearly further work needed to fully understand these  
81 methods at low temperature where the conductivity is most difficult to predict  
82 (e.g. where the effect of isotopic disorder is maximised). Work reported by, e.g.  
83 Sellan et al. (2010), Hu et al. (2011) and Beck et al. (2013) is a significant step  
84 in this direction. Nevertheless, under the high temperature conditions inter-  
85 esting for core-mantle interaction the various computational approaches are  
86 in good agreement and this motivates the current study, which has the aim of  
87 using atomic scale simulation to probe the variation of thermal conductivity  
88 in  $D''$ .

89 Before outlining our approach it is important to note that all these calcula-  
90 tions only capture the portion of heat transport caused by interactions be-  
91 tween lattice vibrations (phonons). This lattice conductivity is believed to  
92 dominate in insulating solids like the mantle silicates and we neglect the elec-  
93 tronic conductivity (important in metals, see Pozzo et al., 2012) and radiative  
94 heat transport, which is expected to be altered by the iron spin transition  
95 at high pressure (see Lin et al., 2013, for a recent review). The importance  
96 of the radiative heat transport is disputed (Hofmeister, 1999; Keppler et al.,

97 2008; Goncharov et al., 2008), but this process will contribute a maximum of  
98 50% of the total conductivity (5 W/mK, Keppler et al., 2008), and probably  
99 much less (0.5 W/mK, Goncharov et al., 2008) in perovskite, and certainly in  
100 post-perovskite (Goncharov et al., 2010).

## 101 2 Methodology

102 We use the so-called direct scheme (Müller-Plathe, 1997; Nieto-Draghi and  
103 Avalos, 2003; Stackhouse and Stixrude, 2010) and invoke non-equilibrium  
104 molecular dynamics to calculate the thermal conductivity of perovskite and  
105 post-perovskite. In this method, physical reality is inverted in the sense that  
106 one imposes a heat flux leading to a thermal gradient (instead of a thermal  
107 gradient leading to a heat flux). The single crystal thermal conductivity  $k$  is  
108 then given by the ratio of the time-averages of the heat flux  $\langle J \rangle$  across a unit  
109 area and the temperature gradient  $\langle dT/dx \rangle$ :

$$110 \quad k = -\frac{\langle J \rangle}{\langle dT/dx \rangle}. \quad (1)$$

111 The heat-flux is imposed by virtual elastic scatters between two atoms in sep-  
112 arated sections of a long simulation cell. The atom with the highest kinetic  
113 energy in the designated cold section and the one with the lowest kinetic en-  
114 ergy in the hot section swap their momenta, effectively transferring heat from  
115 the cold to the hot section (see Stackhouse and Stixrude, 2010, for details).  
116 In order to avoid the high computational costs and system-size limitations  
117 one encounters using density functional theory (DFT), which are particularly  
118 heavy for the large unit cells of perovskite and post-perovskite, we primarily

119 made use of the two established interatomic potential parameterisations of  
120 Murakami et al. (2004) and Oganov et al. (2000). The choice of interatomic  
121 potential is critical to the success of our calculations and we note that a recent  
122 appraisal of 27 possible choices found that the Oganov et al. (2000) model and  
123 similar parameterisations were the most successful (Chen et al., 2012). The  
124 Murakami et al. (2004) model was not included in the study of Chen et al.  
125 (2012). In order to undertake these calculations we modified the code GULP  
126 (Gale and Rohl, 2003) to implement the direct scheme for arbitrarily complex  
127 systems. The use of interatomic potentials allowed us to perform simulations  
128 with up to 11,520 atoms while maintaining predictive power. System-size ef-  
129 fects were corrected by extrapolating to infinite cell size (Schelling et al., 2002)  
130 and by checking convergence on the cross-sectional area (see below). We also  
131 perform DFT simulations of smaller supercells as a test of the interatomic  
132 potentials. These calculations were performed with a modified version of the  
133 VASP code (Stackhouse and Stixrude, 2010).

134 To determine the cell parameters as a function of pressure and temperature  
135 we first performed equilibrium molecular dynamics (MD) for both phases at a  
136 constant pressure and constant temperature using the modified Nosé-Hoover  
137 thermostat (Melchionna et al., 1993) in  $3 \times 3 \times 3$  super-cells. We used a time-  
138 step of 1 fs and the thermo- and barostat parameters both set to 0.05. After  
139 equilibration for 5 ps the time averages over a production run of 20 ps were  
140 used. The resulting parameters (pressure, temperature, unit cell parameters)  
141 are tabulated the Supplementary Information. These parameters were used to  
142 calculate cell volumes for the non-equilibrium molecular dynamics runs used  
143 to calculate the thermal conductivity.

144 NEMD simulations were performed at a constant volume and a constant tem-

145 perature using a Nosé-Hoover-thermostat (Nosé, 1984; Hoover, 1985) with a  
 146 thermostat parameter of 0.05 and time-step of 1 fs. After 5 ps equilibration  
 147 with MD, we started the NEMD simulation which ran for 100 ps. Following  
 148 convergence testing (Figure 1) energy was swapped every 20 fs (i.e., every 20th  
 149 time-step). This established a thermal gradient across the simulation cell, and  
 150 the temperatures of the slices within our simulation cell reached a constant  
 151 temperature after about 30 ps. To calculate  $k$  the simulation cell of dimen-  
 152 sions  $N \times D \times D$  was divided into  $2N$  slices each containing an equal numbers  
 153 of atoms. As shown in Figure 2 we fitted weighted straight lines following  
 154 York (1966, 1967) and calculated errors of our time-averages of temperatures  
 155 and energy-flux with the blocking method (Flyvberg and Petersen, 1989). The  
 156 thermal gradients in the simulation cells were fitted to the central 33% of all  
 157 slices between the hot and cold slice. However, for the smallest cells ( $N \times 3 \times 3$   
 158 when  $N = 6$  and 8) we excluded only the hot and cold slice for the fitting  
 159 procedure. The same weighted linear fitting method was used to extrapolate  
 160 from finite cell-length to infinite cell length (Schelling et al., 2002), see Figure  
 161 3 for examples, and to calculate the errors on the fitting parameters (slope and  
 162 zero-intersect). We found that the effect of increasing the cross-sectional area  
 163 ( $D \times D$ ) is to reduce the thermal conductivity. As shown in Figure 3, converged  
 164 results can be obtained for a  $2 \times 2$  unit cell cross-sectional area for perovskite  
 165 (irrespective of direction), a  $2 \times 1$  unit cell ( $b \times c$ ) for the conductivity along  
 166  $a$  in post-perovskite and  $3 \times 1$  unit cell ( $a \times c$ ) along  $b$  in post-perovskite. We  
 167 used these values for the DFT simulations while for the interatomic potential  
 168 simulations we used  $3 \times 3$  cross-sectional areas to give full convergence.

169 In order to begin to explore the effect of iron-(II) impurities on thermal con-  
 170 ductivity we performed some simulations with the interatomic potentials with

171 randomly chosen magnesium ions replaced with iron (with “iron” in the sim-  
172 ulations being simply a magnesium atom with an atomic weight of 56 g/mol).  
173 These simulations, which are only possible to such low concentrations (down  
174 to 1 % of Mg-sites occupied with Fe) because of the large size of the simulation  
175 cells, should allow us to capture the leading effect of the inclusion of a vari-  
176 able amount of iron in perovskite and post-perovskite on the lattice thermal  
177 conductivity. We do not, however, capture the possibility that the spin tran-  
178 sition in iron ions could dramatically alter the radiative contribution to the  
179 conductivity or the potential effect of other impurities such as aluminium or  
180 iron-(III). While provisional, these calculations highlight an important ben-  
181 efit of the use of computationally efficient interatomic potential models: as  
182 long as they can be validated for pure systems using the predictive power of  
183 DFT they can be used to probe the effect of a wide range phenomena such as  
184 solid-solution, defects (including grain boundaries) and impurities on thermal  
185 conductivity.

186 Geophysically, the thermal conductivity is of interest because it controls the  
187 movement of heat and we complete our study by combining our calculated val-  
188 ues of  $k$  for single crystal perovskite and post-perovskite with previous models  
189 of texture and temperature in  $D''$  (Walker et al., 2011) to build a model of  
190 CMB heat flux. We concentrate on a simple model where the temperature, tex-  
191 ture and phase distribution is fixed and consider how different assumptions  
192 for the state of the lowermost mantle alter the heat flux. In a more sophis-  
193 ticated model changing the heat flux would lead to changes in temperature  
194 that would alter the distribution of perovskite and post-perovskite, the pat-  
195 tern of convection and, in turn, that of conductivity and introduce a number  
196 of feedback mechanisms. In calculating the heat flux for plausible models of

197 the lower mantle, without allowing these feedbacks or necessarily generating  
198 a model that is self consistent, we aim to determine how changes in lowermost  
199 mantle conductivity might alter deep mantle convection. We do not attempt to  
200 directly model the effect of variable and anisotropic conductivity on deep man-  
201 tle convection because current knowledge of how perovskite or post-perovskite  
202 deform is not sufficiently advanced for this task. In order to proceed we recall  
203 that, in three dimensions, the heat flux  $q_i$  in direction  $x_i$  ( $i = 1, 3$ ) is given by  
204 Fourier's law:

$$205 \quad q_i = -K_{ij} \frac{dT}{dx_j}, \quad (2)$$

206 where  $\mathbf{K}$  is the second order thermal conductivity tensor for the polycrystal  
207 and  $T$  is the temperature. The repeated index on the right hand side implies  
208 a summation for values  $j = 1, 3$ . In order to calculate the heat flux across the  
209 thermal boundary layer above the CMB we therefore need to combine two  
210 models: one for the thermal conductivity of the rock forming the lowermost  
211 mantle and one for its temperature. Full details of these two models are given  
212 in the Supplementary Information but, briefly, they consist of the following  
213 components. The one-dimensional geotherm of Stacey and Davis (2008) and  
214 local temperature perturbations taken from Simmons et al. (2009) is used to  
215 calculate the thermal gradients in the layer above the CMB. This model is  
216 identical to that used by Walker et al. (2011) to evaluate the phase stability  
217 and lattice preferred orientation (LPO, calculated using the VPSC code of  
218 Lebensohn and Tomé, 1993) in  $D''$  (a model which used data from: Mitrovica  
219 and Forte, 2004; Oganov and Ono, 2004; Simmons et al., 2009; Forte et al.,  
220 2013). To calculate the bulk conductivity,  $\mathbf{K}$ , we take the mean of the Voigt  
221 and Reuss bounds of single crystal conductivities,  $\mathbf{k}$ , taking account of the tem-  
222 perature dependant phase transition between perovskite and post-perovskite

223 and either assuming  $D''$  is isotropic, or that it exhibits an LPO as modelled  
224 by Walker et al. (2011).

### 225 **3 Results**

226 Results of the atomic scale simulations are summarised in Figures 4 and 5 with  
227 further details given in the Supplementary Information. Both phases show the  
228 expected decrease in conductivity with increasing temperature and increase  
229 in conductivity with increasing pressure. Post-perovskite is consistently more  
230 conducting than perovskite. Both sets of interatomic potentials give good  
231 agreement with the results from DFT, however, the extrapolations to infinite  
232 cell-size differ in terms of the resulting anisotropy. Nevertheless, DFT and in-  
233 teratomic potentials give values within error of each other for the isotropic av-  
234 erage thermal conductivity. To capture the effect of pressure and temperature  
235 on the thermal conductivity we fitted the temperature-dependence of our data  
236 (along all crystallographic axes) with functions of the form:  $k \propto \alpha + \beta/\sqrt{T}$ ,  
237 and used a linear fit to interpolate between the pressures. This leads to a  
238 four-parameter equation we use to describe our results:

$$239 \quad k = \alpha_0 + \alpha_P \cdot P + \frac{\beta_0 + \beta_P \cdot P}{\sqrt{T}}. \quad (3)$$

240 The parameters  $\alpha_0$ ,  $\alpha_P$ ,  $\beta_0$  and  $\beta_P$  for both phases and potential models are  
241 given as a function of direction in the crystal in Table 1.

242 As expected, the result of including iron in our calculations is to reduce the  
243 thermal conductivity. However, as shown in Figure 6, the reduction is vari-  
244 able between phase, crystallographic direction and interatomic potential and

245 rapidly saturates with increasing iron content. Our approach probably gives  
246 a lower bound on the effect of iron impurities (as additional changes in the  
247 atomic interactions associated with the difference in chemistry of iron and  
248 magnesium will increase any anharmonicity and thus the magnitude of the  
249 phonon scattering). Indeed, the reduction in thermal conductivity in per-  
250 ovskite is about half of the 50% reported by Manthilake et al. (2011). The  
251 reason for this discrepancy is probably the presence of  $\text{Fe}^{3+}$  in these experi-  
252 ments (and in the mantle) and we note that our approach could be used to  
253 study this in more detail if suitable transferable interatomic potentials for  
254 these impurities were to be produced. In the meantime, our results show that  
255 thermal conductivity can vary quickly with the addition of a small quantity  
256 of impurities, but that this effect can change and saturate as the impurity  
257 concentration grows. This non-linear behaviour needs to be considered if ex-  
258 perimental results, such as those of Manthilake et al. (2011), are extrapolated  
259 to other impurity contents.

260 In order to gain further confidence in our approach we compare the calculated  
261 conductivity with all the available experimental determinations of thermal  
262 conductivity in  $\text{MgSiO}_3$  perovskite (Osako and Ito, 1991; Goncharov et al.,  
263 2010; Manthilake et al., 2011; Ohta et al., 2012) in Figure 5a. We derive a  
264 conductivity that is slightly ( $< 2$  W/mK) lower than the 26 GPa experimen-  
265 tal data (Manthilake et al., 2011) and agrees with the lower bound of low  
266 precision provisional data from Goncharov et al. (2010) at 125 GPa. Further-  
267 more, there is good agreement with new 300 K data above 80 GPa (Ohta  
268 et al., 2012). Early experiments by Osako and Ito (1991) at ambient condi-  
269 tions give a thermal conductivity of 5 W/mK. This is substantially lower than  
270 our results of  $14 \pm 1$  W/mK under these conditions and is not compatible with

271 the 26 GPa experimental data (Manthilake et al., 2011). This discrepancy  
272 may be due to the presence of a large number of defects in the metastable  
273 perovskite sample measured at low pressure leading to substantial phonon  
274 scattering and a reduction in thermal conductivity or to the effect of decom-  
275 pressed grain boundaries. For post-perovskite there are no experimental data  
276 above 300 K (Ohta et al., 2012). However, the agreement with the 300 K data  
277 and with DFT results (Figure 5b) lends support to the results of the present  
278 calculations.

279 Our results show that post-perovskite conducts heat more easily than per-  
280 ovskite but what are the geophysical implications? Figure 7 shows the thermal  
281 conductivity along the mantle geotherm of Stacey and Davis (2008); for most  
282 of the lower mantle increasing pressure (which increases thermal conductiv-  
283 ity) overcomes the effect of increasing temperature (which decreases it). In  
284 the thermal boundary layer above the CMB the rapid increase in temperature  
285 leads to a decrease in conductivity for both perovskite and post-perovskite, but  
286 post-perovskite still conducts heat 50% faster than perovskite. Another factor  
287 that can lower the conductivity is the presence of impurities (e.g. Fe or Al)  
288 but this effect is hard to quantify in the lowermost mantle as we do not know  
289 how these impurity elements partition between perovskite, post-perovskite  
290 and periclase. However, the saturation of the change in thermal conductivity  
291 with relatively small quantities of iron could suggest that the impurity effect  
292 is homogeneous across the lowermost mantle as compositionally pure phases  
293 are unlikely. Figure 7 also illustrates a second potentially important difference  
294 between the two phases. Thermal conductivity in perovskite is nearly isotropic  
295 but there could be a strong anisotropy for post-perovskite.

296 To illustrate the potential importance of these results we modelled heat flux

297 in the thermal boundary layer above the CMB. We quantify the effects of  
298 temperature dependent thermal conductivity, the increase in thermal con-  
299 ductivity across the phase transition and anisotropic thermal conductivity in  
300 post-perovskite, and compare these effects with the expected variation in tem-  
301 perature in  $D''$ . To do this we evaluate the heat flux on a  $5^\circ$  by  $5^\circ$  grid using  
302 models of the thermal conductivity and temperature field described above. We  
303 evaluate the three components of the temperature gradient by finite difference  
304 of the temperature model described in detail in the Supplementary Informa-  
305 tion, which also includes full results for all our heat flux models. The chosen  
306 geotherm (Stacey and Davis, 2008) implies a baseline CMB heat flux for a  
307 1D isotropic Earth that is  $\sim 40\%$  higher if it is controlled by post-perovskite  
308 compared to a perovskite controlled case. The absolute values reported in the  
309 S.I. are largely controlled by the temperature drop across the CMB and should  
310 only be considered as a reference point in the current work; choosing a differ-  
311 ent geotherm will change the absolute values of the heat flux. However, the  
312 temperature of the core and lowermost mantle is poorly constrained, and we  
313 thus focus on how the heat flux varies across the lowermost mantle rather than  
314 the total heat flux out of the core. We emphasise that these results cannot sim-  
315 ply be scaled to account for a different temperature field or for different heat  
316 production rates in the core or mantle because the model includes important  
317 non-linear effects. We address this topic in more detail in the Conclusions,  
318 below.

320 The spatial pattern of heat flux across the CMB has the potential to influence  
321 convection in the outer core and thus the pattern and evolution of the Earth's  
322 magnetic field (Biggin et al., 2012). This may control the patterns of geomag-  
323 netic reversals (Glatzmaier et al., 1999), lead to a distinctive pattern of high  
324 magnetic flux (Gubbins et al., 2007) and even control how the inner core grows  
325 (Aubert et al., 2008). Even with uniform thermal conductivity hot regions of  
326  $D''$  will lead to low, and cold regions to high, heat flux. Previous workers have  
327 used this information with tomographic images to set a spatially varying heat  
328 flux boundary condition at the CMB for models of the geodynamo (Glatz-  
329 maier et al., 1999; Gubbins et al., 2007). Our data and models confirm that  
330 temperature variation in  $D''$  is the most important control on variation in heat  
331 flux but modifies this view in two important ways. First, the temperature de-  
332 pendence of the thermal conductivity will lead to a further increase in the  
333 heat flux into cold regions and a decrease into hotter regions. Our tempera-  
334 ture model has a range of  $\pm 500$  K from the value defined by the geotherm and  
335 this dominates the pattern of radial heat flux through  $D''$ , which is positively  
336 skewed as the area covered by hot material is smaller than the area covered  
337 by cooler mantle (Figure 8). Changing the conductivity (by comparing models  
338 with a constant 10 W/mK conductivity with those of temperature dependent  
339 conductivity controlled by perovskite) shows that the pattern of high heat  
340 flux in cold areas remains but the skewness increases slightly. A larger effect  
341 is seen when comparing perovskite with post-perovskite. For post-perovskite  
342 dominated lowermost mantle the maximum, mean and modal values of local  
343 heat flux all increase compared to the perovskite case and its distribution

344 broadens. Going from perovskite to post-perovskite increases the maximum  
345 heat flux from 0.04 to 0.06 W/m<sup>2</sup>. A second effect arises from the positive  
346 Clapeyron slope of the phase transition (Hirose et al., 2006) meaning that  
347 post-perovskite is expected to be found in colder regions of D''. This leads  
348 to an interesting mixed phase case (where the phase, and thus thermal con-  
349 ductivity, depends on the temperature) and results in the high maximum and  
350 high modal flux as the post-perovskite case but reduces the heat flux in hotter  
351 regions giving a strongly bimodal heat flux distribution (Figure 8c and d).  
352 Together these two effects will, for any assumed relationship between mantle  
353 temperature and seismic velocity, substantially stretch and modify the range  
354 of heat flux variation, enhancing the potential for mantle control on convection  
355 in the core and thus on the magnetic field.

356 As well as spatial variation on how quickly the core is cooled, the conduc-  
357 tivity step across the perovskite to post-perovskite transition can change the  
358 behaviour of the mantle itself. Geodynamic models show that increasing the  
359 thermal conductivity of D'' increases the size of plumes from the CMB (Nali-  
360 boff and Kellogg, 2006; Tosi et al., 2010). In two-dimensional models of mantle  
361 convection increasing the conductivity across the phase transition gives higher  
362 velocity downwellings and larger asymmetry of the convective planform com-  
363 pared to cases where the conductivity of the two phases are identical (Hunt  
364 et al., 2012; Tosi et al., 2013). The increase in thermal conductivity across the  
365 phase transition is thus expected to be crucial for convection in the mantle  
366 and core. Intriguingly, this may be a transitory effect over the history of the  
367 Earth (e.g. Oganov and Ono, 2004; Kameyama and Yuen, 2006). In the past  
368 it is likely that the mantle was warmer, suppressing the formation of post-  
369 perovskite close to the CMB and reducing the heat flux variation. In the future

370 the core and mantle could be cooler, perhaps with a thick post-perovskite layer  
371 everywhere above the core. We expect the three regimes to yield measurably  
372 different dynamics, for example changing the nature of plumes rising from the  
373 lowermost mantle (Matyska and Yuen, 2006), and it would be interesting to  
374 know if this produced a signature in the palaeomagnetic or tectonic records.  
375 Depending on size and internal structure, larger or cooler terrestrial planets  
376 could enter the ‘future Earth’ regime more quickly while smaller or warmer  
377 planets may never develop into a mixed phase regime.

378 Changing anisotropy of conductivity across the phase transition may also be  
379 important. Seismic studies (e.g., Lay and Young, 1991; Kendall and Silver,  
380 1996; Nowacki et al., 2010, 2011) show that  $D''$  is elastically anisotropic and  
381 this is likely to be the signature of lattice preferred orientation (LPO) of  
382 post-perovskite generated by solid-state deformation from mantle convection  
383 (Panning and Romanowicz, 2004; Merkel et al., 2007; Wenk et al., 2011; Walker  
384 et al., 2011; Nowacki et al., 2013). If correct, the bulk thermal conductivity  
385 of post-perovskite bearing  $D''$  material must also be anisotropic reflecting the  
386 LPO and single crystal conductivity. A similar argument has been made for the  
387 upper mantle where seismic anisotropy is believed to originate from the flow-  
388 induced reorientation of olivine. This is proposed to alter the conductive heat  
389 flux in regions with LPO developed by past or present convection leading to  
390 cooling of old conductive lithospheric roots (Mimouni and Rabinowicz, 1988)  
391 and to fast conduction parallel to strain and deformation induced weakening  
392 (Tommasi et al., 2001; Gibert et al., 2003). As the conductive anisotropy of  
393 olivine is similar in magnitude to that calculated for post-perovskite, similar  
394 arguments can be made for  $D''$ . It turns out that anisotropy plays a minor role  
395 in altering the radial CMB heat flux but can, as discussed in the supplementary

396 material, rotate the heat flux vector and thus change its horizontal components  
397 in a way that is dependent on the active slip systems. Figure 9 shows one  
398 interesting effect in the South East Pacific, close to the possible source of  
399 the Galápagos hot spot (flow in this region is discussed in more detail by  
400 Forte et al., 2013). As illustrated in the cartoon (Figure 9e), anisotropy has  
401 the effect causing heat to traverse across the temperature gradient oblique to  
402 the maximum slope, rather than to flow directly down the thermal gradient  
403 parallel to the direction of maximum decreases in temperature, as expected  
404 in the isotropic case. This has the effect causing the horizontal components  
405 of the heat flux, when viewed from the surface, to be reversed, leading to  
406 conduction towards the plume increasing its buoyancy. We emphasise that  
407 heat is still conducted from hot to cold; what changes is that the heat is no  
408 longer conducted towards the coldest location as expected for the isotropic  
409 case. What happens to the heat flux into the base of the plume if it shifts on  
410 the CMB? Immediately after this movement some of the conductive heating  
411 of the plume base is lost, potentially reducing its buoyancy until the texture  
412 has time to evolve. This suggests that there may be a resistance to movement  
413 of the base of a plume across the CMB caused by the development of LPO and  
414 anisotropic conductivity in  $D''$ . This might contribute to the apparent fixity  
415 of the locations of plumes through geological time. However, quantification  
416 of this effect awaits fully anisotropic dynamic modelling of convection and  
417 texture development in the lowermost mantle.

## 418 5 Conclusions

419 Although the conductivities of perovskite and post-perovskite are both within  
420 the historical range of estimates, we argue that the change in conductivity  
421 and its anisotropy across the phase transition have important implications for  
422 the dynamics of the core and mantle. In our simplified models including the  
423 higher thermal conductivity of post-perovskite increases the heat flux across  
424 the CMB by almost 40%, implying a change in core or mantle temperature if  
425 this were permitted to vary in the model. Even though our models maximise  
426 the effect of anisotropy the global effect is a minor increase or decrease in the  
427 total heat flux. Locally, the effect may be more significant, but the details of  
428 the depend on the active slip system. Our approach is simplified and should  
429 only be taken as an illustration of some of the effects of variable thermal con-  
430 ductivity at the CMB. The model makes use of a fixed temperature field as  
431 input rather than the more challenging approach of attempting to construct a  
432 self-consistent thermal model based on heat production in the mantle and core.  
433 More importantly, there is no feedback between the conductivity, flow field and  
434 resulting distribution of perovskite and post-perovskite. While it is possible  
435 to build a self-consistent global model based on a radial viscosity profile and  
436 mapping between density and temperature (e.g. Forte and Woodward, 1997;  
437 Glišović et al., 2012), in the lowermost mantle lateral variations, exemplified  
438 by the perovskite to post-perovskite phase transition with its steep Clapeyron  
439 slope, makes such an approach difficult. Other important effects that would  
440 have to be considered include the viscosity and chemistry of  $D''$  and the pos-  
441 sibility of phase separation between (Mg,Fe)O and post-perovskite. Models  
442 with softer post-perovskite (Hunt et al., 2009; Ammann et al., 2010; Dobson

443 et al., 2012) give a higher heat flux (Tosi et al., 2010; Nakagawa and Tack-  
444 ley, 2011) and chemical impurities can decrease the conductivity (Manthilake  
445 et al., 2011) and potentially its lateral variation. On the other hand, (Mg,Fe)O  
446 could segregate into bands or layers parallel to the CMB and this could open  
447 new conductive paths parallel to these layers. In this case the anisotropy of  
448 conductivity in the lower most mantle would increase reenforcing the pattern  
449 shown in Figure 9. New, more sophisticated convective models are required  
450 if we are to explore the dynamical consequences of a textured and heteroge-  
451 neous  $D''$  including lenses of rheologically weak, chemically distinct, thermally  
452 conducting and anisotropic post-perovskite.

## 453 **6 Acknowledgments**

454 We acknowledge the use of high performance computing provided by UCL  
455 Research Computing, the Advanced Computing Research Centre, University  
456 of Bristol (<http://www.bris.ac.uk/acrc/>) and of HECToR, the UK's national  
457 high-performance computing service, which is provided by UoE HPCx Ltd  
458 at the University of Edinburgh, Cray Inc and NAG Ltd, and funded by the  
459 Office of Science and Technology through EPSRC's High End Computing  
460 Programme. The research leading to these results has received funding from  
461 NERC (NE/H007636/1) and the European Research Council under the Euro-  
462 pean Union's Seventh Framework Programme (FP7/2007-2013)/ ERC Grant  
463 agreement 240473 "CoMITAC". We thank Carlos Tomé and Ricardo Leben-  
464 sohn for making their VPSC code available to us.

465 **References**

- 466 Ammann, M. W., Brodholt, J. P., Wookey, J., Dobson, D. P., 2010. First-  
467 principles constraints on diffusion in lower-mantle minerals and a weak D''  
468 layer. *Nature* 465, 462 – 465.
- 469 Aubert, J., Amit, H., Hulot, G., Olson, P., 2008. Thermochemical flows couple  
470 the Earth's inner core growth to mantle heterogeneity. *Nature* 454, 758 –  
471 762.
- 472 Beck, M., Haigis, V., Schilling, F., Jahn, S., 2013. Thermal conductivity of  
473 (Mg,Fe)O from ambient to deep mantle conditions. *Mineralogical Magazine*  
474 77, 674.
- 475 Biggin, A. J., Steinberger, B., Aubert, J., Suttie, N., Holme, R., Torsvik, T. H.,  
476 van der Meer, D. G., van Hinsbergen, D. J. J., 2012. Possible links between  
477 long-term geomagnetic variations and whole-mantle convection processes.  
478 *Nature Geoscience* 5, 526 – 533.
- 479 Chen, Y., Chernatynskiy, A., Brown, D., Schelling, P. K., Artacho, E.,  
480 Phillpot, S. R., 2012. Critical assessment of classical potentials for MgSiO<sub>3</sub>  
481 perovskite with application to thermal conductivity calculations. *Physics of*  
482 *the Earth and Planetary Interiors* 210-211, 75 – 89.
- 483 Cohen, R. E., 1998. Thermal conductivity of MgO at high pressures. *The*  
484 *Review of High Pressure Science and Technology* 7, 160 – 162.
- 485 Dalton, D. A., Hsieh, W.-P., Hohensee, G. T., Cahill, D. G., Goncharov, A. F.,  
486 2013. Effect of mass disorder on the lattice thermal conductivity of MgO  
487 periclase under pressure. *Scientific Reports* 3, art. num. 2400.
- 488 de Koker, N., 2009. Thermal conductivity of MgO periclase from equilibrium  
489 first principles molecular dynamics. *Physical Review Letters* 103, 125902.
- 490 de Koker, N., 2010. Thermal conductivity of MgO periclase at high pressure:

491 Implications for the D'' region. *Earth and Planetary Science Letters* 292 (3-  
492 4), 392–398.

493 Dekura, H., Tsuchiya, T., Tsuchiya, J., 2013. Ab initio lattice thermal con-  
494 ductivity of MgSiO<sub>3</sub> perovskite as found in earth's lower mantle. *Physical*  
495 *Review Letters* 110, 025904.

496 Dobson, D. P., McCormack, R., Hunt, S. A., Ammann, M. W., Weidner,  
497 D. J., Li, L., Wang, L., 2012. The relative strength of perovskite and post-  
498 perovskite in the system NaCoF<sub>3</sub>. *Mineralogical Magazine* 76, 925 – 932.

499 Flyvberg, H., Petersen, H., 1989. Error estimates on averages of correlated  
500 data. *Journal of Chemical Physics* 91, 461–466.

501 Forte, A. M., Simmons, N. A., Grand, S. P., 2013. Constraints on 3-D seis-  
502 mic models from global geodynamic observables: Implications for the global  
503 mantle convective flow. In: Romanowicz, B., Dziewonski, A. (Eds.), *Treatise*  
504 *on Geophysics. Seismology and the Structure of the Earth, Second Edition.*  
505 Vol. 1. Elsevier, pp. 805 – 858.

506 Forte, A. M., Woodward, R. L., 1997. Seismic-geodynamic constraints on  
507 three-dimensional structure, vertical flow, and heat transfer in the mantle.  
508 *Journal of Geophysical Research* 192, 17981 – 17994.

509 Gale, J. D., Rohl, A. L., 2003. The general utility lattice program (GULP).  
510 *Molecular Simulation* 29 (5), 291 – 341.

511 Gibert, B., Seipold, U., Tommasi, A., Mainprice, D., 2003. Thermal diffu-  
512 sivity of upper mantle rocks: Influence of temperature, pressure, and the  
513 deformation fabric. *Journal of Geophysical Research* 108, 2359.

514 Glatzmaier, G. A., Coe, R. S., Hongre, L., Roberts, P. H., 1999. The role of  
515 the Earth's mantle in controlling the frequency of geomagnetic reversals.  
516 *Nature* 401, 885 – 890.

517 Glišović, P., Forte, A. M., Moucha, R., 2012. Time-dependent convection mod-

518 els of mantle thermal structure constrained by seismic tomography and geo-  
519 dynamics: implications for mantle plume dynamics and CMB heat flux.  
520 *Geophysical Journal International* 190, 785 – 815.

521 Goncharov, A., Struzhkin, V., Montoya, J., Kharlamova, S., Kundargi, R.,  
522 Siebert, J., Badro, J., Antonangeli, D., Ryerson, F., Mao, W., 2010. Effect  
523 of composition, structure, and spin state on the thermal conductivity of the  
524 earth’s lower mantle. *Physics of the Earth and Planetary Interiors* 180 (3-4),  
525 148–153.

526 Goncharov, A. F., Beck, P., Struzhkin, V. V., Haugen, B. D., Jacobsen, S. D.,  
527 2009. Thermal conductivity of lower-mantle minerals. *Physics of the Earth*  
528 *and Planetary Interiors* 174, 24 – 32.

529 Goncharov, A. F., Haugen, B. D., Struzhkin, V. V., Beck, P., Jacobsen, S. D.,  
530 2008. Radiative conductivity in the Earth’s lower mantle. *Nature* 456, 231  
531 – 233.

532 Gubbins, D., 2003. Thermal core-mantle interactions: theory and observations.  
533 In: Dehant, V., Creager, K. C., Karato, S.-I., Zatman, S. (Eds.), *Earth’s*  
534 *Core: Dynamics, Structure, Rotation*. Vol. 31 of *Geodynamics Series*. AGU,  
535 pp. 163 – 179.

536 Gubbins, D., Willis, A. P., Sreenivasan, B., 2007. Correlation of Earth’s mag-  
537 netic field with lower mantle thermal and seismic structure. *Physics of the*  
538 *Earth and Planetary Interiors* 162, 256 – 260.

539 Haigis, V., Salanne, M., Jahn, S., 2012. Thermal conductivity of MgO, MgSiO<sub>3</sub>  
540 perovskite and post-perovskite in the Earth’s deep mantle. *Earth and Plan-*  
541 *etary Science Letters* 355-356, 102 – 108.

542 Hirose, K., Sinmyo, R., Sata, N., Ohishi, Y., 2006. Determination of post-  
543 perovskite phase transition boundary in MgSiO<sub>3</sub> using Au and MgO internal  
544 pressure standards. *Geophysical Research Letters* 33, L01310.

545 Hofmeister, A. M., 1999. Mantle values of thermal conductivity and the  
546 geotherm from phonon lifetimes. *Science* 283, 1699 – 1706.

547 Hofmeister, A. M., 2008. Inference of high thermal transport in the lower  
548 mantle from laser-flash experiments and the damped harmonic oscillator  
549 model. *Physics of the Earth and Planetary Interiors* 170, 201 – 206.

550 Hoover, W. G., 1985. Canonical dynamics: Equilibrium phase-space distribu-  
551 tions. *Physical Review A* 31, 1695–1697.

552 Hu, L., Evans, W. J., Keblinski, P., 2011. One-dimensional phonon effects in  
553 direct molecular dynamics method for thermal conductivity determination.  
554 *Journal of Applied Physics* 110, 113511.

555 Hunt, S. A., Davies, D. R., Walker, A. M., McCormack, R., Wills, A. S.,  
556 Dobson, D. P., Li, L., 2012. On the increase in thermal diffusivity caused by  
557 the perovskite to post-perovskite phase transition and its implications for  
558 mantle dynamics. *Earth and Planetary Science Letters* 319-320, 96 – 105.

559 Hunt, S. A., Weidner, D. J., Li, L., Wang, L., Walte, N. P., Brodholt, J. P.,  
560 Dobson, D. P., 2009. Weakening of calcium iridate during its transformation  
561 from perovskite to post-perovskite. *Nature Geoscience* 2, 794 – 797.

562 Kameyama, M., Yuen, D. A., 2006. 3-D convection studies on the thermal  
563 state in the lower mantle with post-perovskite phase transition. *Geophysical*  
564 *Research Letters* 33, L12S10.

565 Kendall, J.-M., Silver, P. G., 1996. Constraints from seismic anisotropy on the  
566 nature of the lowermost mantle. *Nature* 381, 409 – 412.

567 Keppler, H., Dubrovinsky, L. S., Narygina, O., Kantor, I., 2008. Optical ab-  
568 sorption and radiative thermal conductivity of silicate perovskite to 125  
569 gigapascals. *Science* 322, 1529 – 1532.

570 Lay, T., Hernlund, J., Buffett, B. A., 2008. Core-mantle boundary heat flow.  
571 *Nature Geoscience* 1, 25 – 32.

- 572 Lay, T., Young, C. J., 1991. Analysis of seismic SV waves in the core's penum-  
573 bra. *Geophysical Research Letters* 18, 1373–1376.
- 574 Lebensohn, R. A., Tomé, C. N., 1993. A self-consistent anisotropic approach  
575 for the simulation of plastic deformation and texture development of poly-  
576 crystals: Application to zirconium alloys. *Acta Metallurgica et Materialia*  
577 41 (9), 2611 – 2624.
- 578 Lin, J.-F., Speziale, S., Mao, Z., Marquardt, H., 2013. Effects of the elec-  
579 tronic spin transitions of iron in lower-mantle minerals: implications for  
580 deep-mantle geophysics and geochemistry. *Reviews of Geophysics* 51, 244 –  
581 275.
- 582 Manthilake, G. M., de Koker, N., Frost, D. J., McCammon, C. A., 2011. Lattice  
583 thermal conductivity of lower mantle minerals and heat flux from Earth's  
584 core. *Proceedings of the National Academy of Science* 108, 17901 – 17904.
- 585 Matyska, C., Yuen, D. A., 2006. Lower mantle dynamics with the post-  
586 perovskite phase change, radiative thermal conductivity, temperature- and  
587 depth-dependent viscosity. *Physics of the Earth and Planetary Interiors* 154,  
588 196 – 207.
- 589 Melchionna, S., Ciccotti, G., Holian, B. L., 1993. Hoover NPT dynamics for  
590 systems varying in shape and size. *Molecular Physics* 78, 533–544.
- 591 Merkel, S., McNamara, A. K., Kubo, A., Speziale, S., Miyagi, L., Meng,  
592 Y., Duffy, T. S., Wenk, H.-R., 2007. Deformation of (Mg,Fe)SiO<sub>3</sub> post-  
593 perovskite and D'' anisotropy. *Science* 316, 1729 – 1732.
- 594 Mimouni, A., Rabinowicz, M., 1988. The old continental shields stability re-  
595 lated to mantle convection. *Geophysical Research Letters* 15, 68 – 71.
- 596 Mitrovica, J. X., Forte, A. M., 2004. A new inference of mantle viscosity  
597 based upon joint inversion of convection and glacial isostatic adjustment  
598 data. *Earth and Planetary Science Letters* 225, 177 – 189.

599 Müller-Plathe, F., 1997. A simple nonequilibrium molecular dynamics method  
600 for calculating the thermal conductivity. *Journal of Chemical Physics* 106,  
601 6082 – 6085.

602 Murakami, M., Hirose, K., Kawamura, K., Sata, N., Ohishi, Y., 2004. Post-  
603 perovskite phase transition in  $\text{MgSiO}_3$ . *Science* 304, 855 – 858.

604 Nakagawa, T., Tackley, P. J., 2011. Effects of low-viscosity post-perovskite  
605 on thermo-chemical mantle convection in a 3-D spherical shell. *Geophysical*  
606 *Research Letters* 38, L04309:1–6.

607 Naliboff, J. B., Kellogg, L. H., 2006. Dynamic effects of a step-wise increase  
608 in thermal conductivity and viscosity in the lowermost mantle. *Geophysical*  
609 *Research Letters* 33, L12S09.

610 Nieto-Draghi, C., Avalos, J. B., 2003. Non-equilibrium momentum exchange  
611 algorithm for molecular dynamics simulation of heat flow in multicomponent  
612 systems. *Molecular Physics* 101, 2303–2307.

613 Nosé, S., 1984. A unified formulation of the constant temperature molecular  
614 dynamics methods. *Journal of Chemical Physics* 81, 511–519.

615 Nowacki, A., Walker, A. M., Wookey, J., Kendall, J.-M., 2013. Evaluating  
616 post-perovskite as a cause of  $D''$  anisotropy in regions of palaeosubduction.  
617 *Geophysical Journal International* 192, 1085 – 1090.

618 Nowacki, A., Wookey, J., Kendall, J.-M., 2010. Deformation of the lowermost  
619 mantle from seismic anisotropy. *Nature* 467, 1091 – 1094.

620 Nowacki, A., Wookey, J., Kendall, J.-M., 2011. New advances in using seismic  
621 anisotropy, mineral physics and geodynamics to understand deformation in  
622 the lowermost mantle. *Journal of Geodynamics* 52, 205 – 228.

623 Oganov, A. R., Brodholt, J. P., Price, G. D., 2000. Comparative study of quasi-  
624 harmonic lattice dynamics, molecular dynamics and Debye model applied  
625 to  $\text{MgSiO}_3$  perovskite. *Physics of the Earth and Planetary Interiors* 122,

626 277–288.

627 Oganov, A. R., Ono, S., 2004. Theoretical and experimental evidence for a  
628 post-perovskite phase of  $\text{MgSiO}_3$  in Earth's  $D''$  layer. *Nature* 430, 445 –  
629 448.

630 Ohta, K., Yagi, T., Taketoshi, N., Hirose, K., Komabayashi, T., Baba, T.,  
631 Ohishi, Y., Hernlund, J., 2012. Lattice conductivity of  $\text{MgSiO}_3$  perovskite  
632 and post-perovskite at the core–mantle boundary. *Earth and Planetary Sci-*  
633 *ence Letters* 349-350, 109 – 115.

634 Osako, M., Ito, E., 1991. Thermal diffusivity of  $\text{MgSiO}_3$  perovskite. *Geophys-*  
635 *ical Research Letters* 18, 239 – 242.

636 Panning, M., Romanowicz, B., 2004. Inferences on flow at the base of Earth's  
637 mantle based on seismic anisotropy. *Science* 303, 351 – 353.

638 Pozzo, M., Davies, C., Gubbins, D., Alfè, D., 2012. Thermal and electrical  
639 conductivity of iron at Earth's core conditions. *Nature* 485, 355 – 358.

640 Schelling, P. K., Phillpot, S. R., Keblinski, P., 2002. Comparison of atomic-  
641 level simulation methods for computing thermal conductivity. *Physical Re-*  
642 *view B* 65, 144306:1–12.

643 Sellan, D. P., Landry, E. S., Turney, J. E., McGaughey, A. J. H., Amon, C. H.,  
644 2010. Size effects in molecular dynamics thermal conductivity predictions.  
645 *Physical Review B* 81, 214305.

646 Simmons, N. A., Forte, A. M., Grand, S. P., 2009. Joint seismic, geodynamic  
647 and mineral physical constraints on three-dimensional mantle heterogeneity:  
648 Implications for the relative importance of thermal versus compositional  
649 heterogeneity. *Geophysical Journal International* 177, 1284 – 1304.

650 Stacey, F. D., Davis, P. M., 2008. *Physics of the Earth*, 4th Edition. Cambridge  
651 University Press.

652 Stackhouse, S., Stixrude, L., 2010. Theoretical methods for calculating the

653 lattice thermal conductivity of minerals. *Reviews in Mineralogy and Geo-*  
654 *chemistry* 71, 253 – 269.

655 Stackhouse, S., Stixrude, L., Karki, B. B., 2009. Thermal conductivity of MgO  
656 and MgSiO<sub>3</sub> perovskite at lower mantle conditions. EOS: Transactions of  
657 the American Geophysical Union Fall meeting supplement, abstract number  
658 MR13C–05.

659 Stackhouse, S., Stixrude, L., Karki, B. B., 2010. Thermal conductivity of per-  
660 iclase (MgO) from first principles. *Physical Review Letters* 104, 208501.

661 Tang, X., Dong, J., 2009. Pressure dependence of harmonic and anharmonic  
662 lattice dynamics in MgO: A first-principles calculation and implications for  
663 lattice thermal conductivity. *Physics of the Earth and Planetary Interiors*  
664 174, 33 – 38.

665 Tommasi, A., Gibert, B., Seipold, U., Mainprice, D., 2001. Anisotropy of ther-  
666 mal diffusivity in the upper mantle. *Nature* 411, 783 – 786.

667 Tosi, N., Čadež, O., Yuen, D. A., 2010. Dynamical consequences in the lower  
668 mantle with the post-perovskite phase change and strongly depth-dependent  
669 thermodynamic and transport properties. *Earth and Planetary Science Let-*  
670 *ters* 298, 229 – 243.

671 Tosi, N., Yuen, D. A., de Koker, N., Wentzcovitch, R. M., 2013. Mantle dy-  
672 namics with pressure- and temperature-dependent thermal expansivity and  
673 conductivity. *Physics of the Earth and Planetary Interiors* 217, 48 – 58.

674 Walker, A. M., Forte, A. M., Wookey, J., Nowacki, A., Kendall, J.-M., 2011.  
675 Elastic anisotropy of  $D''$  predicted from global models of mantle flow. *Geo-*  
676 *chemistry Geophysics Geosystems* 12, Q10006.

677 Wenk, H.-R., Cottar, S., Tomé, C. N., McNamara, A., Romanowicz, B., 2011.  
678 Deformation in the lowermost mantle: From polycrystal plasticity to seismic  
679 anisotropy. *Earth and Planetary Science Letters* 306, 33 – 45.

680 York, D., 1966. Least-squares fitting of a straight line. *Canadian Journal of*  
681 *Physics* 44, 1079–1086.

682 York, D., 1967. The best isochoron. *Earth and Planetary Science Letters* 2,  
683 479–482.

Table 1

Parameters for Equation 3 describing the variation in thermal conductivity (in W/mK) of perovskite and post-perovskite with pressure (in GPa), temperature (in K) and direction. Results for individual pressures and temperatures are given in the Supplementary Information.

Phase and direction	$\alpha_0$	$\alpha_P$	$\beta_0$	$\beta_P$
Perovskite, isotropic average <sup>a</sup>	-1.1676	-0.0014	211.19	2.6212
Perovskite, parallel to <i>a</i> -axis <sup>a</sup>	-0.0349	0.0029	244.30	1.4842
Perovskite, parallel to <i>c</i> -axis <sup>a</sup>	3.0495	-0.0597	144.97	4.8951
Post-perovskite, isotropic average <sup>a</sup>	-3.5501	-0.0254	678.95	3.0203
Post-perovskite, parallel to <i>a</i> -axis <sup>a</sup>	-13.0000	0.0100	1309.60	0.5600
Post-perovskite, parallel to <i>b</i> -axis <sup>a</sup>	7.8513	-0.1018	0.5950	7.8658
Post-perovskite, parallel to <i>c</i> -axis <sup>a</sup>	-5.1953	0.0130	727.09	0.6318
Perovskite, isotropic average <sup>b</sup>	-1.0618	0.0105	203.74	2.3210
Perovskite, parallel to <i>a</i> -axis <sup>b</sup>	2.4414	-0.0186	141.20	2.7199
Perovskite, parallel to <i>c</i> -axis <sup>b</sup>	-0.3872	0.0098	328.82	1.5232
Post-perovskite, isotropic average <sup>b</sup>	-16.8163	0.0606	1194.20	0.5096
Post-perovskite, parallel to <i>a</i> -axis <sup>b</sup>	-68.0000	0.3900	4478.00	-19.8900
Post-perovskite, parallel to <i>b</i> -axis <sup>b</sup>	22.1088	-0.1900	-1098.48	14.5315
Post-perovskite, parallel to <i>c</i> -axis <sup>b</sup>	-4.3000	-0.0200	202.90	6.8600

<sup>a</sup> Using the potentials from Oganov et al. (2000)

<sup>b</sup> Using the potentials from Murakami et al. (2004)

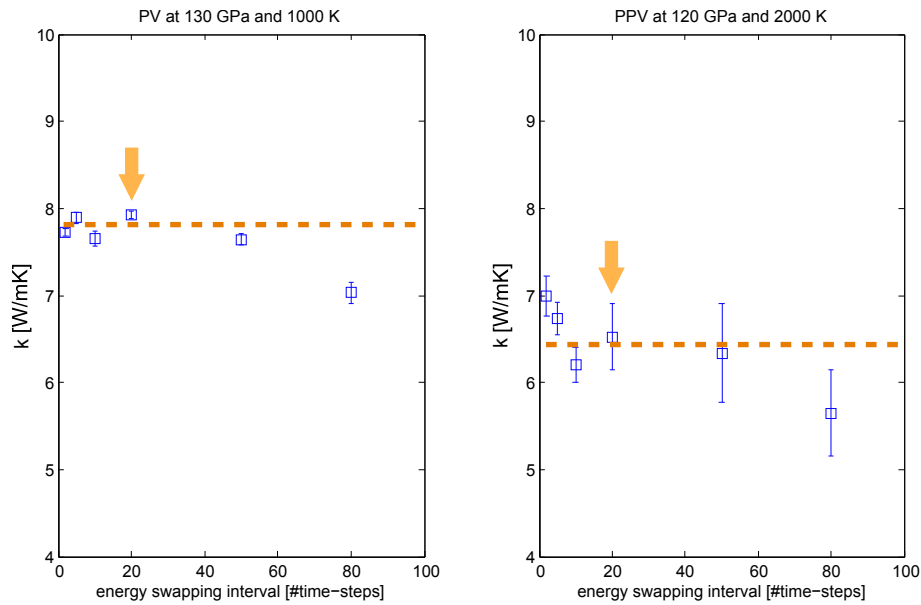


Fig. 1. Thermal conductivity as a function of the generated temperature gradient for different heat exchange intervals. Perovskite (left) at 130 GPa, 1000 K in a  $16 \times 3 \times 3$  supercell and post-perovskite (right) at 120 GPa, 2000 K in a  $12 \times 3 \times 3$  supercell. (The temperature gradient is generated along the  $a$ -axis for both phases). For all but the longest exchange interval (80 fs), perfect linear correlation has been found, confirming the validity of heat equation.

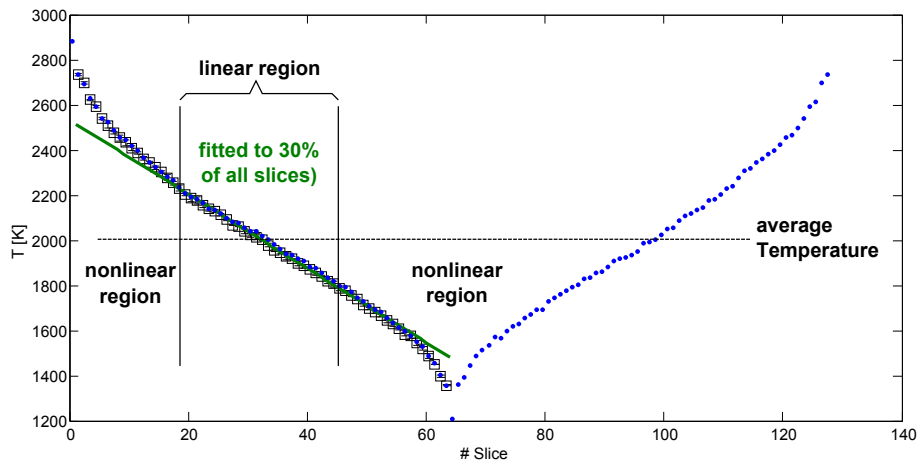


Fig. 2. Temperatures (blue dots; squares are averages between left and right half of simulation cell indicating that steady state has been reached) of the slices across the simulation-cell ( $64 \times 3 \times 3$ , post-perovskite at 120 GPa and 2000 K). Green line: fitted linear thermal gradient across cell after 100 ps of simulation time.

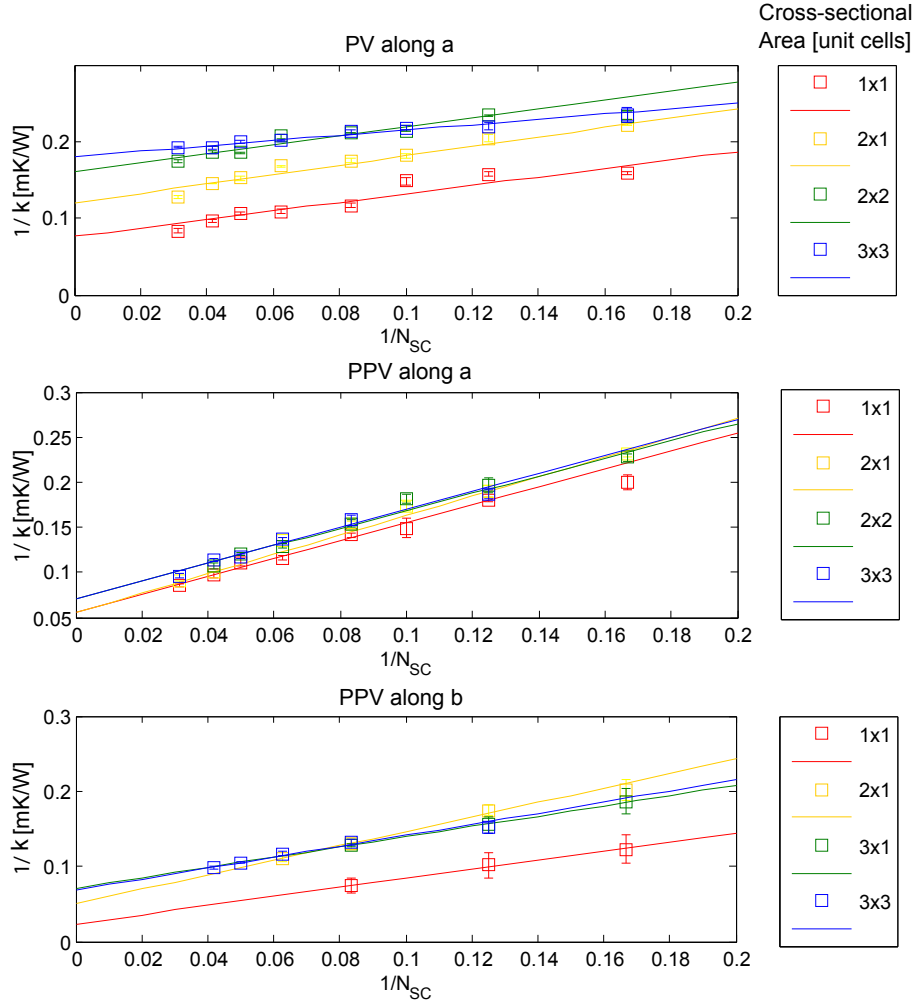


Fig. 3. The effect of the cross-sectional area on the thermal conductivity of perovskite (20 GPa and 2000 K) along  $a$  (top) and post-perovskite (120 GPa and 2000 K) along  $a$  (centre) and  $b$  (bottom) as a function of the simulation-cell length. Squares mark values for different simulation-cell lengths, lines are the linear extrapolations to infinite cell-size (see text for details).

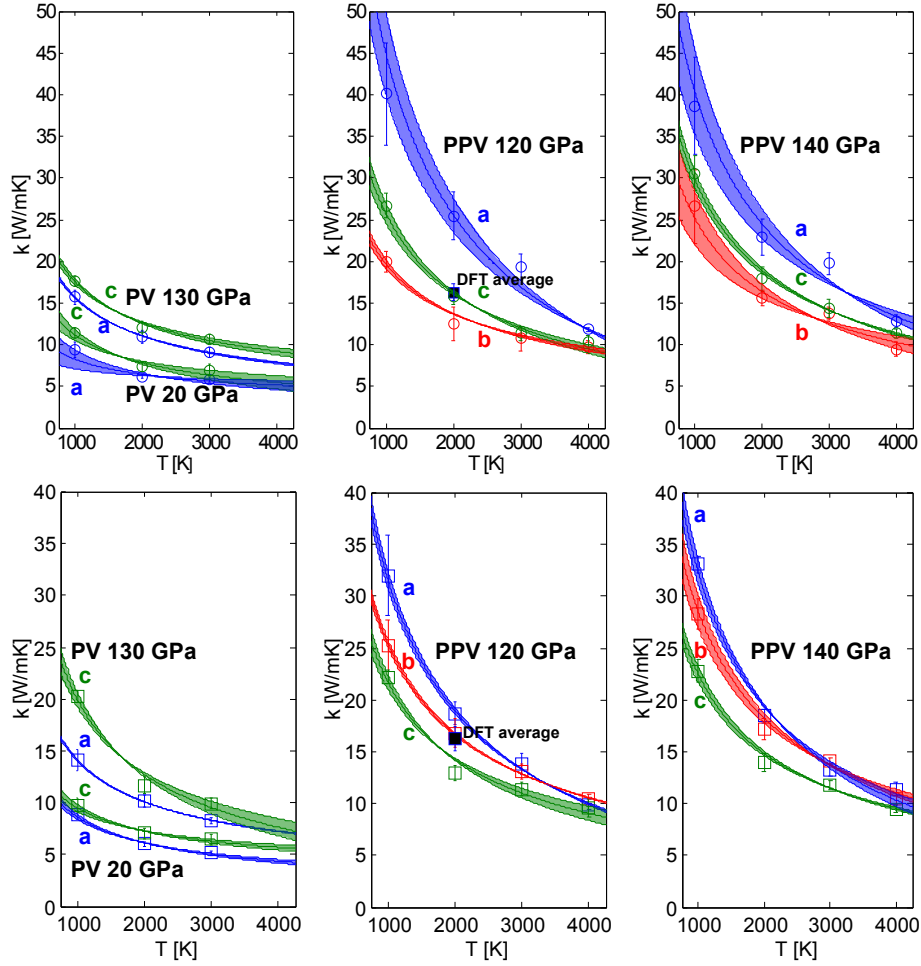


Fig. 4. Thermal conductivities of perovskite and post-perovskite as functions of temperature with the potential from Murakami et al. (2004) (top) and Oganov et al. (2000) (bottom). Shown are the thermal conductivities at different pressures along different crystal axis as marked. Squares are the calculated conductivities with lines being  $1/T^{1/2}$  least-square fits and their appropriate error bounds. Post-perovskite is anisotropic particularly at lower temperatures.

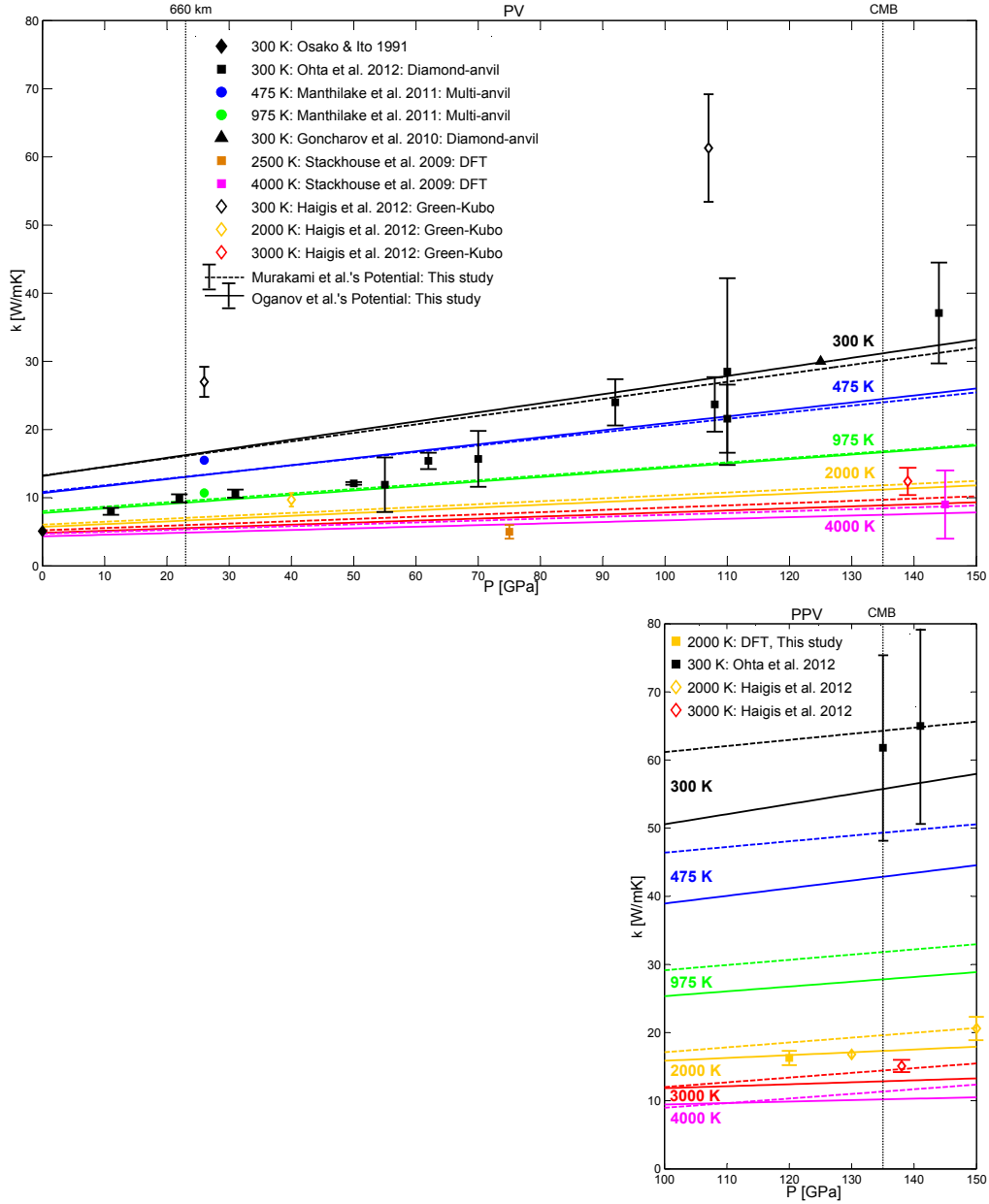


Fig. 5. Comparison of the calculated thermal conductivities of perovskite (a) and post-perovskite (b) as a function of temperature and pressure compared with the available experimental data. Solid and dashed lines: results from non-equilibrium molecular dynamics where, for any pressure, lower conductivities are found with increasing temperature (typical error bars are shown in the key). Symbols: experimental data or results from atomic scale calculations with error bars (colours refer to temperature; the DFT data points shown for perovskite were previously presented by Stackhouse et al. (2009) and will form the basis for a future publication, we do not plot the 300 K, 135 GPa data of Haigis et al. (2012) for post-perovskite because it lies so far from the rest of the plotted data). For the low precision provisional data (Goncharov et al., 2010) the lower bound of the conductivity is shown (the very large errors reported in these experiments are due to lack of knowledge of the conductivity of other components in the sample assembly). Above about 80 GPa our calculations using interatomic potentials agree with all available data for both phases.

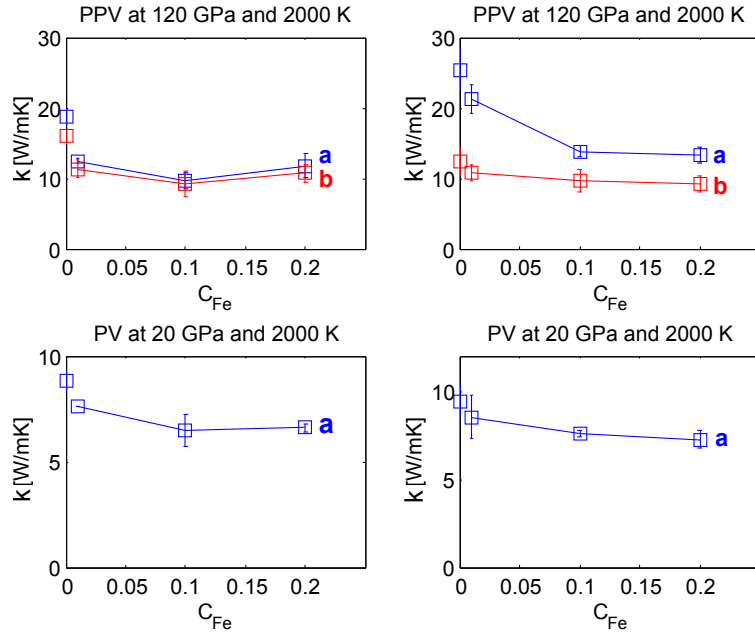


Fig. 6. Thermal conductivities as functions of iron concentration using the potentials from Oganov et al. (2000), left, and Murakami et al. (2004), right. The thermal conductivity quickly saturates with increasing iron concentration.

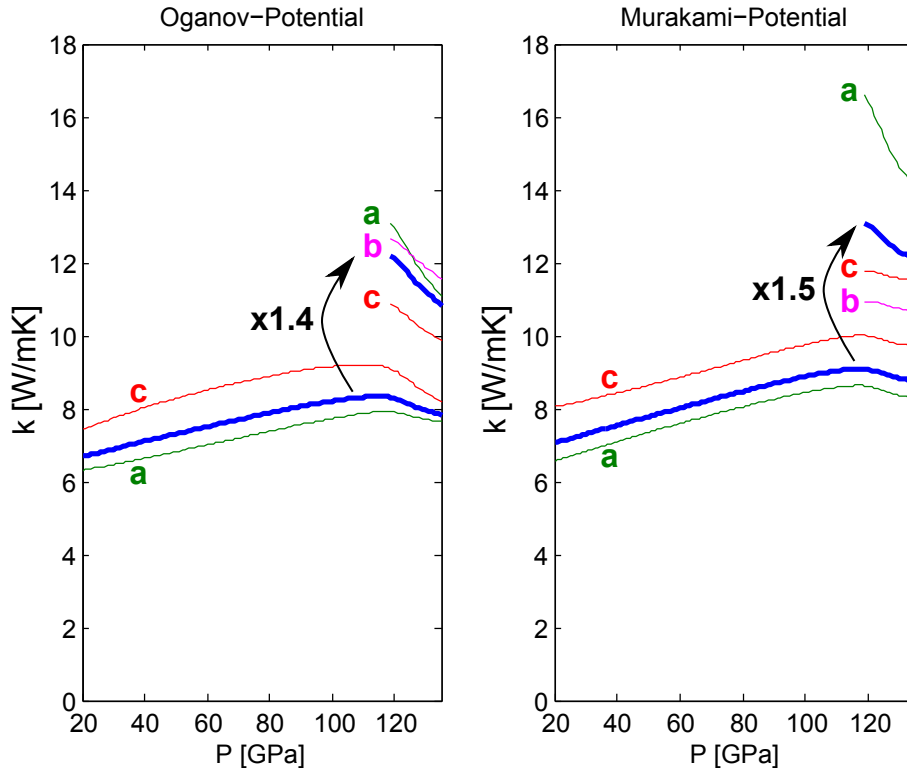


Fig. 7. Calculated single crystal thermal conductivity of perovskite and post-perovskite along a geotherm (Stacey and Davis, 2008). Note the large (factor of 1.5) increase in conductivity across the phase transition and the large anisotropy for post-perovskite exhibited by the potential of Murakami et al.

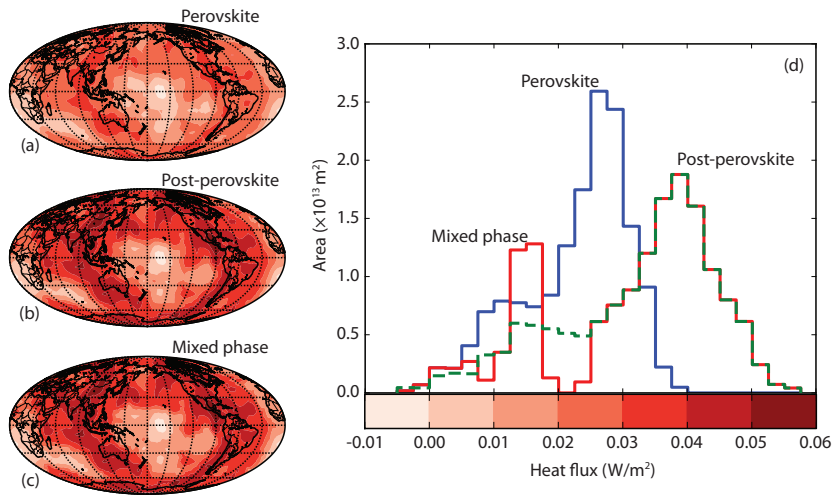


Fig. 8. Calculated radial heat flux distribution across the CMB. (a) – (c) show the spatial variation in heat flux for conductivity dominated by perovskite, post-perovskite and a mixed-phase assemblage, respectively. (d) Histogram of the heat flux distribution showing the low, unimodal distribution for perovskite, the higher unimodal distribution for post-perovskite and the bimodal distribution for the mixed phase case. Integrated CMB heat flux for these three cases are 3.48, 4.93 and 4.83 TW, respectively. Further details of these models are given in the Supplementary Information.

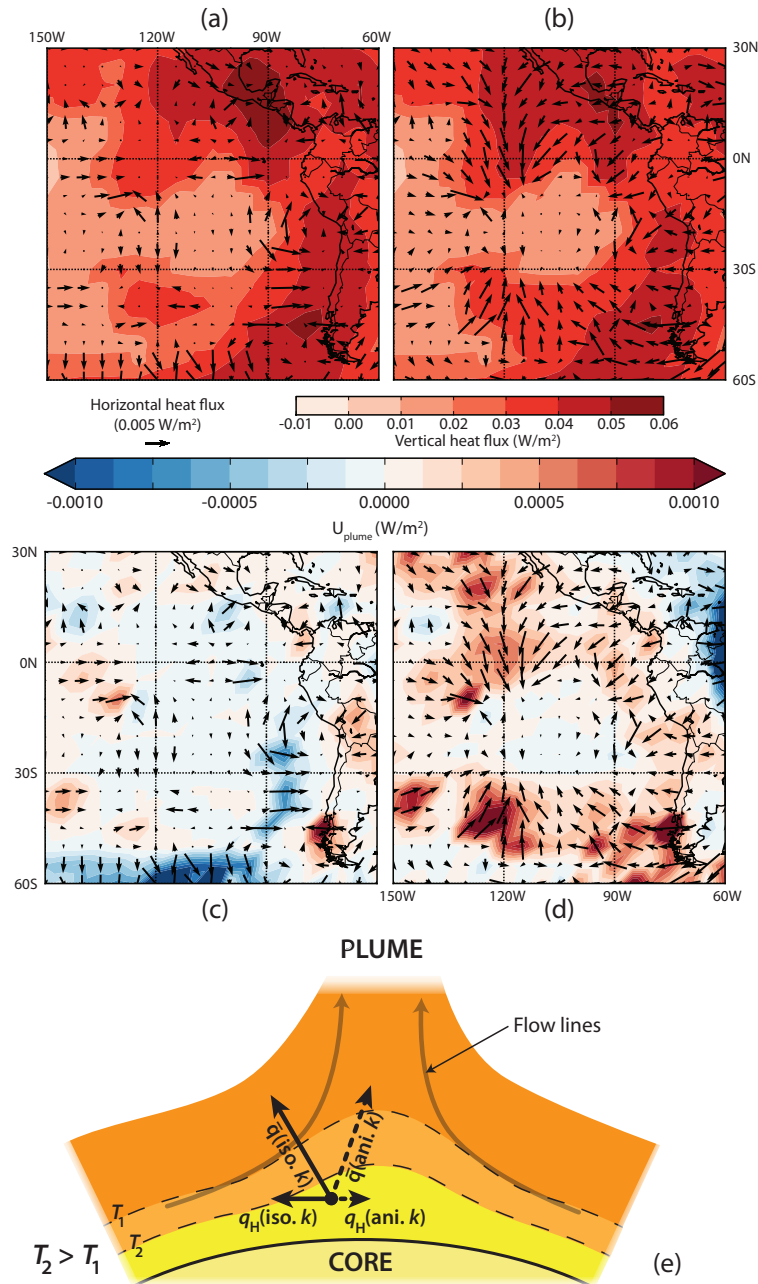


Fig. 9. Calculated heat flux distribution across the CMB around the south east Pacific centred on an up-welling in the TX2008.V2 mantle flow model. Upper panels show the horizontal (arrows) and vertical (red contour fill) component of the heat flux for an isotropic (a; close up of Figure 8c) and anisotropic (b; anisotropy derived from TX2008.V2.P100 polycrystalline deformation model, results for other proposed slip systems can be found in the Supplementary Information). Blue – red contours in the lower panels show the magnitude of the horizontal heat flux resolved in the direction towards the centre of the upwelling,  $U_{\text{plume}}$ , for the isotropic (c) and anisotropic (d) cases. (e) Cartoon showing how a change in the direction of the heat flux vector results in a change in the horizontal components.